

The effect of the earth pressure coefficients on the runout of granular material

Marina Pirulli ^{a,*}, Marie-Odile Bristeau ^b, Anne Mangeney ^c, Claudio Scavia ^a

^a Department of Structural and Geotechnical Engineering, Politecnico di Torino, Corso Duca degli Abruzzi, 24, Torino 10129, Italy

^b Institut National de Recherche en Informatique et en Automatique, Projet BANG, BP 105, Le Chesnay Cedex 78153, France

^c Département de Modélisation Physique et Numérique, Institut de Physique du Globe de Paris, Université Paris 7, 4 Place Jussieu, Paris 75252, France

Received 24 October 2005; received in revised form 20 June 2006; accepted 26 June 2006

Available online 23 August 2006

Abstract

In the framework of a better territory risk assessment and decision making, numerical simulation can provide a useful tool for investigating the propagation phase of phenomena involving granular material, like rock avalanches, when realistic geological contexts are considered.

Among continuum mechanics models, the numerical model SHWCIN uses the depth averaged Saint Venant approach, in which the avalanche thickness (H) is very much smaller than its extent parallel to the bed (L). The material is assumed to be incompressible and the mass and the momentum equations are written in a depth averaged form.

The SHWCIN code, based on the hypothesis of isotropy of normal stresses ($\sigma_{xx} = \sigma_{yy} = \sigma_{zz}$), has been modified (new code: RASH^{3D}) in order to allow for the assumption of anisotropy of normal stresses ($\sigma_{xx} = K\sigma_{zz}$; $\sigma_{yy} = K\sigma_{zz}$).

A comparison among the results obtained by assuming isotropy or anisotropy is given through the back analysis of a set of laboratory experiments [Gray, J.M.N.T., Wieland, M., Hutter, K., 1999. Gravity-driven free surface flow of granular avalanches over complex basal topography. *Proceedings of the Royal Society of London, Series A* 455(1841)] and of a case history of rock avalanche (Frank slide, Canada).

The carried out simulations have also underlined the importance of using a different earth pressure coefficient value (K) for directions of convergence and of divergence of the flux.

© 2006 Elsevier Ltd. All rights reserved.

Keywords: Rock avalanche; Numerical analysis; Earth pressure coefficients; Granular material; Back analysis

1. Introduction

The evaluation of risk due to large landslides requires the understanding of two fundamental problems: the initiation and the runout of the event. Even though the triggering of the landslide is a primary problem, which is not yet completely solved, the runout, which consists in the flowing and stopping phases of the mass, is here analysed.

As a matter of fact, reliable predictions of runout are an important step in estimating the extension of the hazardous areas and in helping to reduce losses and to avoid exceedingly

conservative decisions regarding the development of an area (see for instance, Wilkinson et al., 2002).

Numerical simulation should provide a useful tool for investigating, within realistic geological contexts, the runout of large landslides.

A noteworthy type of modelling is based on a discontinuum mechanics approach (e.g. Strack and Cundall, 1984; Cundall, 1988; Walton et al., 1988; Will and Konietzky, 1998), in which the runout mass is modelled as an assembly of particles moving down along a surface. However, nowadays this approach still presents some limitations that in some way compromise a satisfactory application to large movement analysis.

The numerical models more promising from the application point of view are today based on a continuum mechanics approach (e.g. Hungr, 1995; Chen and Lee, 2000; Denlinger

* Corresponding author. Fax: +39 0115644899.

E-mail address: marina.pirulli@polito.it (M. Pirulli).

and Iverson, 2004; Mangeney-Castelnau et al., 2003; Pirulli, 2005).

In 1989, Savage and Hutter applied for the first time the depth averaged Saint Venant equations to the analysis of propagation of a granular mass. This was the first step to the development of some numerical models of runout having a different solver but all based on a continuum mechanics approach and on Saint Venant equations (i.e. Gray et al., 1999; Chen and Lee, 2000; Iverson and Denlinger, 2001; McDougall and Hungr, 2004).

Continuum mechanics models treat granular materials as a continuum. An “apparent” fluid, whose rheological properties do not correspond to any of the landslide real components, is used to simulate expected bulk behaviour of the landslide.

It is also important to underline that there are important differences between fluid and earth material. In a fluid the lateral pressure coefficient K always equals 1. If the bulk of the flowing mass is a dry granular material with friction, the coefficient K may range between the active and passive coefficient K_{act} and K_{pass} (Hungr, 1995).

The value of these coefficients plays an important role in the development of the avalanche runout and deposit shape, as they control how much spreading and contraction of the running mass can occur.

To simplify the resolution of the problem, existing models make different hypotheses concerning the assumed direction along which the shear stress is dominant.

If it is assumed that the predominant motion is in the x -direction, it results that the dominant shearing is parallel to the xz -plane (Fig. 7).

The x -direction is considered by Gray et al. (1999) as the direction of steepest descent, while by McDougall and Hungr (2004) as the direction of the movement.

The Gray et al. (1999) approach is justified for slides moving in a reasonably straight line, which tends to be oriented downslope.

These assumptions destroy the rotational invariance of the earth pressure coefficients, but yield a relatively simple system of equations (i.e. Hutter et al., 1993).

Based on a continuum mechanics approach and on depth averaged equations, the numerical model RASH^{3D}, which is able to run analyses of propagation on a complex topography, is presented in this paper. The source code (SHWCIN, Mangeney-Castelnau et al., 2003), describing granular flows on a simplified topography, was originally developed by Audusse et al. (2000) and Bristeau et al. (2001) to compute Saint Venant equation in hydraulic problems.

To carry out analyses of propagation on a real topography some fundamental changes concerning topology optimization and gravity vector components were necessary to make in the SHWCIN code (Pirulli, 2005).

Further, as the SHWCIN code assumed isotropy of normal stresses, i.e. $\sigma_{xx} = \sigma_{yy} = \sigma_{zz}$, an anisotropy condition has been also numerically implemented. Following the Iverson and Denlinger (2001) approach, a K coefficient which applies in the x and y direction simultaneously has been assumed. Use

of a scalar coefficient ensures frame invariance in the x – y plane and preserves the stress symmetry.

The new upgraded code (RASH^{3D}) has been applied to compare the behaviour of the mass during propagation in conditions of both isotropy and anisotropy. In this paper the obtained results in case of both a laboratory experiment (Gray et al., 1999) and a case history of rock avalanche (Frank slide; 1903, Canada) are presented in detail.

2. Continuum mechanics approach

Continuum mechanics models for rapid landslides use techniques developed for analysis of the flow of fluids in open channels, but there are important differences between fluids and earth materials, even if the latter are saturated and highly disturbed. In addition, landslide paths are often much steeper and more varied than channels considered in most hydraulic calculations and landslide motion is highly unsteady.

Granular material consists of a large assemblage of discrete particles. If the depth and length of the flowing mass are large compared to the dimensions of a typical particle, it is reasonable to treat the involved material as a continuum. In this framework it becomes fundamental to find an “apparent” fluid whose rheological properties are such that the bulk behaviour of the flowing body simulates the expected bulk behaviour of the landslide (Fig. 1). As previously mentioned, the properties of the equivalent fluid do not correspond to those of any of the slide components.

Under these conditions, the motion of the avalanching mass can be described using a model consisting of the balances of mass and momentum, namely

$$\nabla \cdot \mathbf{u} = 0 \quad (1)$$

$$\rho \left(\frac{\partial \mathbf{u}}{\partial t} + \mathbf{u} \cdot \nabla \mathbf{u} \right) = \nabla \cdot \boldsymbol{\sigma} + \rho \mathbf{g} \quad (2)$$

in which $\mathbf{u}(x, y, z, t) = (u(x, y, z, t), v(x, y, z, t), w(x, y, z, t))$ denotes the three-dimensional velocity vector inside the avalanche in a (x, y, z) coordinate system that will be discussed later, $\boldsymbol{\sigma}(x, y, z, t)$ is the Cauchy stress tensor, ρ the mass density, and $\mathbf{g} (= -g(\gamma_x, \gamma_y, \gamma_z))$ the vector of gravitational

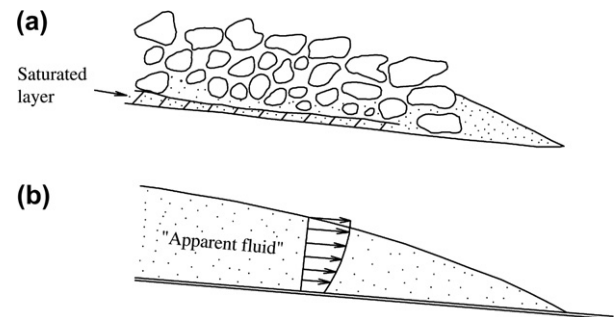


Fig. 1. (a) Scheme of a heterogeneous and complex moving mass; (b) A homogeneous “apparent fluid” replaces the slide mass (modified from Hungr, 1995).

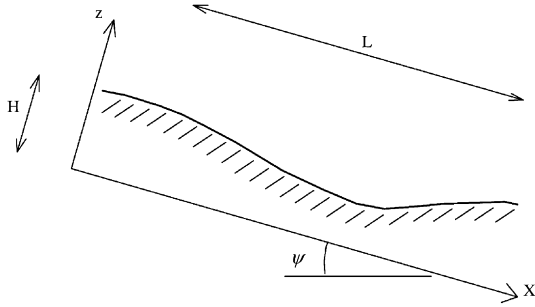


Fig. 2. Depth averaged approximation.

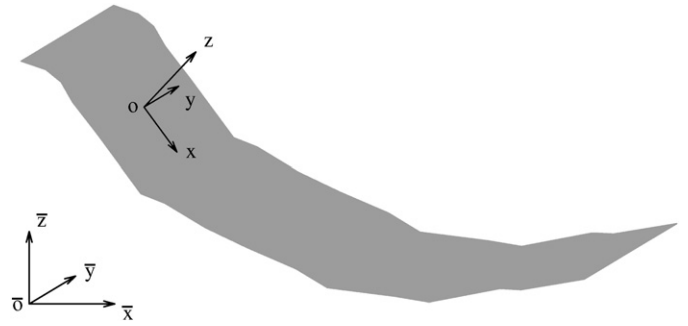


Fig. 3. Representation of fixed reference frame $(\bar{x}, \bar{y}, \bar{z})$ and of reference system linked to the topography (x, y, z) .

acceleration, defined as the projection along the i ($=x,y,z$) direction of a unit vector opposite to \mathbf{g} .

A kinematic boundary condition is imposed on the free surface and an impermeability condition is prescribed at the bottom, that specifies that mass neither enters nor leaves at the base.

During an avalanche, the characteristic length in the flowing direction (L) is generally much larger than the vertical one (e.g. avalanche thickness), H (Fig. 2). Such a long-wave scaling argument has been widely used in derivation of continuum flow models. This leads to depth averaged models governed by generalized Saint Venant equations.

Depth averaging allows us to avoid a complete three-dimensional description of the flow: the complex rheology of the granular material is incorporated in a single term describing the frictional stress that develops at the interface between the flowing material and the rough surface (bed or base).

In the last years, an increased interest on prediction of landslide runout has induced researchers to develop more and more comprehensive numerical models. Based on a continuum mechanics approach, different models have been numerically implemented. These models mainly differ from one another in numerical solver and type of adopted mesh.

3. Numerical model description

The SHWCIN code, based on the classical finite volume approach for solving hyperbolic systems of equations using the concept of cell centred conservative quantities, was originally developed by Audusse et al. (2000) and Bristeau et al. (2001) to describe the flows in rivers, coastal areas or floodings.

The code extension for granular flow analysis was obtained introducing a Coulomb-type friction law and a reference system linked to the topography by Mangeney-Castelnau et al., 2003.

In a reference frame linked to the topography (Fig. 3) and in the hypothesis of isotropy of normal stresses, equations of mass and momentum in the x and y direction read

$$\frac{\partial h}{\partial t} + \text{div}(h\mathbf{u}) = 0 \quad (3)$$

$$\frac{\partial}{\partial t}(hu) + \frac{\partial}{\partial x}(hu^2) + \frac{\partial}{\partial y}(huv) = -\gamma_x gh - \frac{\partial}{\partial x}\left(g\gamma_z \frac{h^2}{2}\right) - \mu g \gamma_z h \frac{u_x}{\|\mathbf{u}\|} \quad (4)$$

$$\frac{\partial}{\partial t}(hv) + \frac{\partial}{\partial x}(huv) + \frac{\partial}{\partial y}(hv^2) = -\gamma_y gh - \frac{\partial}{\partial y}\left(g\gamma_z \frac{h^2}{2}\right) - \mu g \gamma_z h \frac{u_y}{\|\mathbf{u}\|} \quad (5)$$

where $\mathbf{u} = (u, v)$ denotes the depth averaged flow velocity in the reference frame (x, y, z) defined below, h is the fluid depth, $\mu = \tan \delta$, where δ is the basal friction angle.

Due to the isotropy condition, the assumed depth averaged stress tensor is

$$\bar{\sigma} = \begin{pmatrix} \rho g \gamma_z \frac{h}{2} & 0 & 0 \\ 0 & \rho g \gamma_z \frac{h}{2} & 0 \\ 0 & 0 & \rho g \gamma_z \frac{h}{2} \end{pmatrix} \quad (6)$$

and the traction vector $\mathbf{T} = (T_x, T_y, T_z) = -\sigma \cdot \mathbf{n}_b$ where \mathbf{n}_b is the unit vector normal to the bed of the sliding mass, reads

$$\mathbf{T} = \begin{pmatrix} -\mu \rho g \gamma_z h \frac{u}{\|\mathbf{u}\|} \\ -\mu \rho g \gamma_z h \frac{v}{\|\mathbf{u}\|} \\ -\mu \rho g \gamma_z h \end{pmatrix} \quad (7)$$

Dissipation is described by a Coulomb-type friction law relating the norm of the tangential traction $\|\mathbf{T}_t\|$ at the bed to the norm of the normal traction $\|\mathbf{T}_n\| = |T_z| = |\sigma_{zz}|$ at the bed, through the factor μ . In the considered coordinate system, $\sigma_c = \mu \rho g \gamma_z h$ defines the upper bound of the admissible stresses (for detail, see Mangeney-Castelnau et al., 2003).

If $\|\mathbf{T}_t\| \geq \sigma_c$ the mass is flowing following the dynamical equations, if $\|\mathbf{T}_t\| < \sigma_c$ the mass stops and the momentum equations are replaced by $u = 0$. Mangeney-Castelnau et al. (2003) introduces a Dirac distribution of particles at the micro-scale in order to describe the stopping of a granular

mass when the driving forces are under the Coulomb threshold.

The algorithm used in SHWCIN gives a first order of precision in both space and time.

The system of equations is in the code discretized on a general triangular grid with a finite element data structure using a particular control volume which is the median based dual cell. Dual cells C_i are obtained by joining the centres of mass of the triangles surrounding each vertex P_i (Fig. 4). The following notations are used: K_i set of nodes P_j surrounding P_i , A_i area of C_i , Γ_{ij} boundary edge belonging to cells C_i and C_j , L_{ij} length of Γ_{ij} , \mathbf{n}_{ij} unit normal to Γ_{ij} outward to C_i .

The system of Eqs. (3)–(5) can be re-written as

$$\frac{\partial \mathbf{U}}{\partial t} + \text{div } \mathbf{F}(\mathbf{U}) = \mathbf{B}(\mathbf{U}) \quad (8)$$

with

$$\mathbf{U} = \begin{pmatrix} h \\ q_x \\ q_y \end{pmatrix}; \quad \mathbf{F}(\mathbf{U}) = \begin{pmatrix} q_x & q_y \\ \frac{q_x^2}{h} + \frac{g}{2}h^2 & \frac{q_x q_y}{h} \\ \frac{q_x q_y}{h} & \frac{q_y^2}{h} + \frac{g}{2}h^2 \end{pmatrix};$$

$$\mathbf{B}(\mathbf{U}) = \begin{pmatrix} 0 \\ -gh\gamma_x - T_x \\ -gh\gamma_y - T_y \end{pmatrix} \quad (9)$$

where $\mathbf{q} = h\mathbf{u}$.

It is here presented the assumed numerical scheme without details concerning friction terms, these terms are widely treated in Mangeney-Castelnau et al. (2003).

In the finite volume scheme, Eq. (8) assumes the following configuration

$$\mathbf{U}_i^{n+1} = \mathbf{U}_i^n - \sum_{j \in K_i} \alpha_{ij} F(\mathbf{U}_i^n, \mathbf{U}_j^n, \mathbf{n}_{ij}) + \Delta t B(\mathbf{U}_i^n) \quad (10)$$

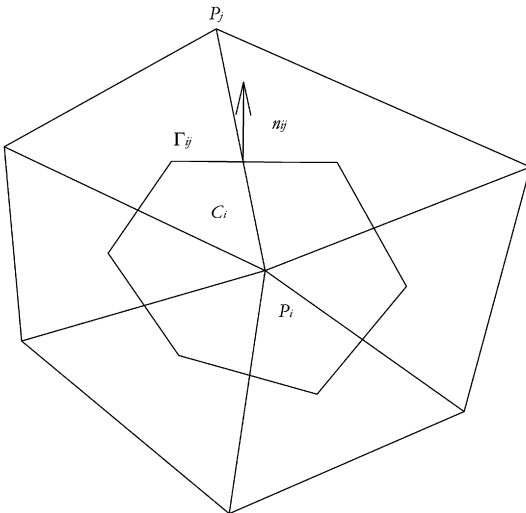


Fig. 4. Triangular finite element mesh (from Mangeney-Castelnau et al., 2003).

with Δt , the time step

$$\alpha_{ij} = \frac{\Delta t L_{ij}}{A_i}$$

$$\mathbf{U}_i^n \cong \frac{1}{A_i} \int_{C_i} \mathbf{U}(t^n, x) dx$$

the approximation of the cell average of the exact solution at time t^n

$$B(\mathbf{U}_i^n) \cong \frac{1}{A_i} \int_{C_i} \mathbf{B}(\mathbf{U}_i^n) dx$$

the approximation of the cell average of the exact source term at time t^n

$$F(\mathbf{U}_i^n, \mathbf{U}_j^n, \mathbf{n}_{ij})$$

an interpolation of the normal component of the flux $\mathbf{F}(\mathbf{U}) \cdot \mathbf{n}_{ij}$ along the edge Γ_{ij} .

The main difficulty is to compute fluxes at the control volumes interfaces Γ_{ij} and to guarantee the overall stability of the method. The computation of these fluxes is made using a kinetic scheme that consists in using a fictitious description of the microscopic behaviour of the system to define numerical fluxes. It is introduced here the main concept of the kinetic scheme used in this model; a complete description of this scheme and its numerical implementations are done by Audusse et al. (2000), Bristeau et al. (2001) and Audusse and Bristeau (2005).

A distribution function of fictitious particles $M(t, x, y, \xi)$ with velocity ξ (here a rectangular function Π) is introduced in order to obtain a linear microscopic kinetic equation equivalent to the macroscopic Eq. (8). The microscopic density M of particle present at time t in the vicinity $\Delta x \Delta y$ of the position (x, y) and with a velocity ξ is defined as

$$M(t, x, y, \xi) = \frac{h(t, x, y)}{c^2} \chi\left(\frac{\xi - \mathbf{u}(t, x, y)}{c}\right) \quad (11)$$

with “fluid density” h , “fluid temperature” proportional to $c^2 = gh/2$ and $\chi(\omega)$ a positive even function defined on \mathcal{R}^2 (Mangeney-Castelnau et al., 2003).

The macroscopic quantities are linked to the microscopic function by the following relations

$$\mathbf{U} = \int_{\mathcal{R}^2} \begin{pmatrix} 1 \\ \xi \end{pmatrix} M(t, x, y, \xi) d\xi \quad (12)$$

$$\mathbf{F}(\mathbf{U}) = \int_{\mathcal{R}^2} \begin{pmatrix} \xi \\ \xi \otimes \xi \end{pmatrix} M(t, x, y, \xi) d\xi \quad (13)$$

$$\mathbf{B}(\mathbf{U}) = g \cdot \int_{\mathcal{R}^2} \begin{pmatrix} 1 \\ \xi \end{pmatrix} \nabla_{\xi} M(t, x, y, \xi) d\xi \quad \text{with } g = (g_x, g_y) \quad (14)$$

These relations imply that the nonlinear system Eqs. (3)–(5) is equivalent to the linear transport equation for the quantity M , for which it is easier to find a simple numerical scheme with good properties

$$\frac{\partial M}{\partial t} + \xi \cdot \nabla_x M - g\gamma \cdot \nabla_\xi M = Q(t, x, y, \xi) \quad (15)$$

for some collision term $Q(t, x, y, \xi)$ which satisfies

$$\int_{\mathcal{R}^2} \left(\frac{1}{\xi} \right) Q(t, x, y, \xi) d\xi = 0 \quad (16)$$

The “collision term” $Q(t, x, y, \xi)$ in this kinetic representation of the Saint Venant equations is neglected in the numerical scheme.

Finally, the discretization of the obtained kinetic equation allows to deduce an appropriate discretization of the macroscopic system. From the microscopic Eq. (15) the formulations of the fluxes defined in Eq. (10) are obtained as follows

$$F(\mathbf{U}_i, \mathbf{U}_j, \mathbf{n}_{ij}) = \mathbf{F}^+(\mathbf{U}_i, \mathbf{n}_{ij}) + \mathbf{F}^-(\mathbf{U}_j, \mathbf{n}_{ij}) \quad (17)$$

$$\mathbf{F}^+(\mathbf{U}_i, \mathbf{n}_{ij}) = \int_{\xi \cdot \mathbf{n}_{ij} \geq 0} \xi \cdot \mathbf{n}_{ij} \left(\frac{1}{\xi} \right) M_i(\xi) d\xi \quad (18)$$

$$\mathbf{F}^-(\mathbf{U}_j, \mathbf{n}_{ij}) = \int_{\xi \cdot \mathbf{n}_{ij} \leq 0} \xi \cdot \mathbf{n}_{ij} \left(\frac{1}{\xi} \right) M_j(\xi) d\xi \quad (19)$$

The simple form of the density function allows analytical resolution of integrals Eqs. (18) and (19) and gives the possibility to directly write a finite volume formula, which therefore avoids using the extra variable ξ in the implementation of the code. The resulting numerical scheme is consistent and conservative.

3.1. Numerical model upgrade

Some changes in the original version (SHWCIN) of the applied code have been necessary to run analyses of propagation on a complex three-dimensional topography.

The obtained code (RASH^{3D}) has been validated for each change through simulation of experimental laboratory tests (Pirulli, 2005).

Firstly it is pointed out that some numerical problems can occur in topology optimization. In SHWCIN a triangular regular mesh, which in the following will be called “structured mesh”, was usually assumed. Through a very simple three-dimensional analysis of a hemi-spherical mass flowing on a horizontal plane it is shown that propagation on a structured mesh does not result symmetric, as it would be expected. The existence of elements having all the same direction originates a preferential direction of propagation of the mass (Fig. 5).

This mesh dependency can be reduced by increasing the number of elements of a structured mesh through a higher discretization. The obtained results underline a considerable increase of the cpu-time without a complete removal of the problem.

An important result was obtained turning to “unstructured mesh”, numerically implemented through a Delaunay triangulation.

It is seen that, assuming the same initial geometry of the experiment considered with a structured mesh, an unstructured mesh is able to reduce the asymmetry of the propagation (Fig. 6). Further, since a huge increment of number of elements is not necessary, the cpu-time remains approximately the same.

As a second aspect, it is underlined that runout of a mass can be deeply influenced by changes in the slope geometry which are very frequent in real cases of rock avalanches. In these cases, it must be taken into account that the gravity vector components (g_x, g_y, g_z) modify along the path as a function of dip and dip direction of the slope and a component having negligible effect in a certain portion of the slope could become predominant in another one.

In SHWCIN gravity vector components were defined for an invariant topography in the y direction. It means that the transversal extension of an assumed topography was considered as the lateral extrusion of a given profile.

To run analyses of propagation on a complex topography it has been necessary to modify the gravity vector components so that a different term (g_x, g_y, g_z) is defined for each point

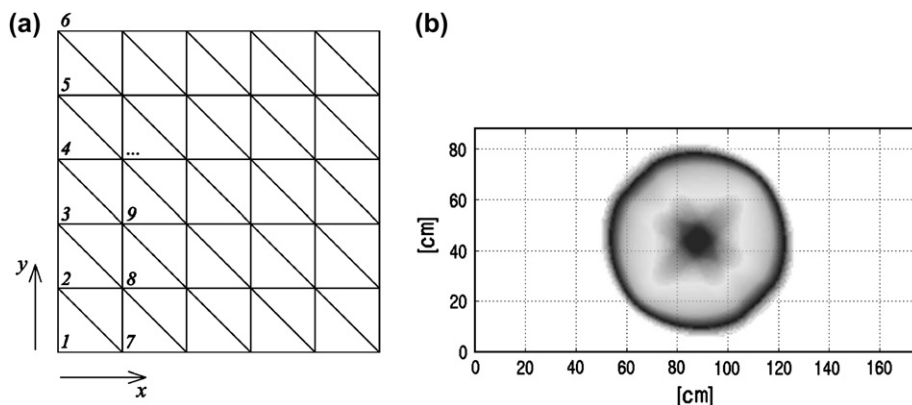


Fig. 5. (a) A structured mesh. (b) Propagation of hemi-spherical mass on horizontal plane at $t = 0.3$ s using a structured mesh.

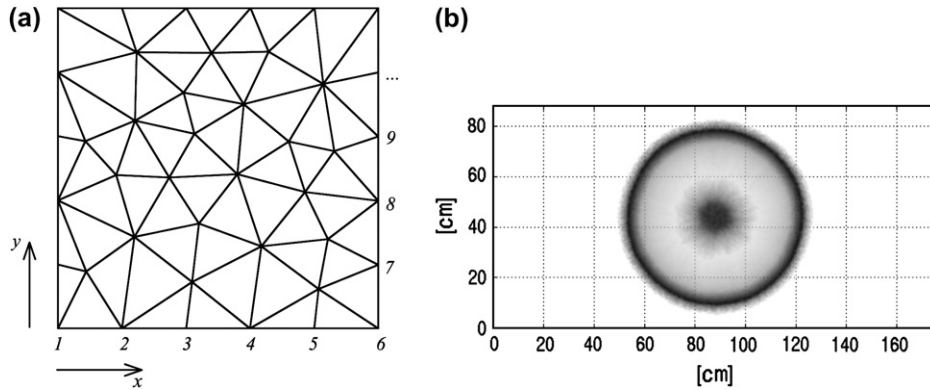


Fig. 6. (a) An unstructured mesh. (b) Propagation of hemispherical mass on horizontal plane at $t = 0.3$ s using an unstructured mesh.

of the mesh as a function of the behaviour that the topography assumes in the vicinity of the considered point (Pirulli, 2005).

Finally the earth pressure coefficients are important to model the mass behaviour in a correct way. As explained in detail in Section 4, in every analysis it is necessary to distinguish between convergence and divergence of the mass and it is fundamental to use a different earth pressure coefficient value (K) for directions of convergence and of divergence of the flux.

A detailed description of the procedure followed to introduce these aspects in the finite volume scheme assumed in the numerical code is widely treated in Pirulli, 2005.

4. Earth pressure coefficients

4.1. Theoretical analysis

The Savage and Hutter theory, which assumes that a very simple state of stress prevails within an avalanche, is here considered. It hypothesizes that, at the base and at the stress free surface of the flowing mass, the normal stresses σ_{xx} and σ_{yy} can be expressed in terms of the overburden normal stress σ_{zz} through Mohr-circle considerations. Its validity through depth is justified by the continuity requirement. The hypothesis that the predominant shearing takes place in surfaces normal to the x – z plane (Fig. 7) allows, as a rough approximation, to assume that the lateral confinement normal stress σ_{yy} is close to a principal stress σ_1 .

Furthermore, it shall be assumed that one of the other principal stresses acting in the (x,z) -surface, σ_2 and σ_3 , equals σ_1 . This is an ad hoc assumption that is not guaranteed by any physical reason, but that reduces the three Mohr-circles that describe all possible combinations of normal stresses and shear stresses to only one Mohr-circle as in two dimensions. Thus, to a given stress state $(\sigma_{xx}^b, \tau_{xz}^b)$, at the base, two Mohr stress circles can be constructed to satisfy both the basal sliding law and the internal yield criterion simultaneously. Their construction is shown in Fig. 8.

The principal stresses, σ_2 and σ_3 in the xz -plane are given by

$$(\sigma_2, \sigma_3) = \frac{1}{2}(\sigma_{xx} + \sigma_{zz}) \pm \frac{1}{2}\sqrt{(\sigma_{xx} - \sigma_{zz})^2 + 4\tau_{xz}^2} \quad (20)$$

and the cross-slope principal stress $\sigma_{yy}(=\sigma_1)$ equals σ_2 or σ_3 , depending on the nature of deformation. Two Mohr stress circles can be constructed that satisfy both the basal sliding law and the internal angle of friction at the same time.

In the original works of Savage and Hutter (1991) the basal normal stress equals σ and the shear stress equals $-\tau_{xz}^b$. The basal downslope normal stress σ_{xx}^b can therefore assume two values, one on the smaller circle, $\sigma_{xx}^b \leq \sigma_{zz}^b$, and one on the larger circle $\sigma_{xx}^b > \sigma_{zz}^b$, that are related to active and passive stress states, respectively. Since there are four possible values

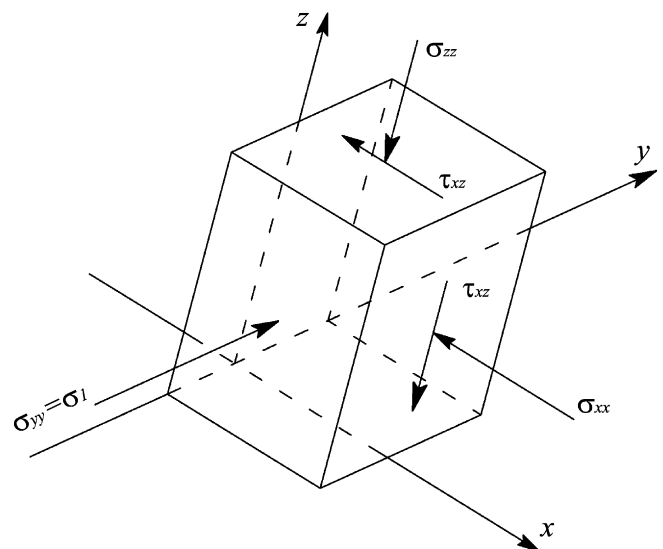


Fig. 7. Infinitesimal cubic element cut out of the avalanche with surface perpendicular to the coordinates. It is assumed that the motion predominantly is in the direction of steepest descent (x) and the dominant shearing is parallel to the xz -plane. This gives rise to the dominant shear stresses τ_{xz} and normal pressures σ_{xx} , σ_{yy} , σ_{zz} . Shear stresses τ_{yz} and τ_{xy} also arise but much smaller than τ_{xz} . Thus σ_{yy} equals approximately to σ_1 , one of the principal stresses (when τ_{yz} and τ_{xy} vanish exactly then σ_{yy} is exactly σ_1). The other two principal stresses, σ_2 and σ_3 , act on surface elements of which the surface normals lie in the xz -plane (from Savage and Hutter, 1989).

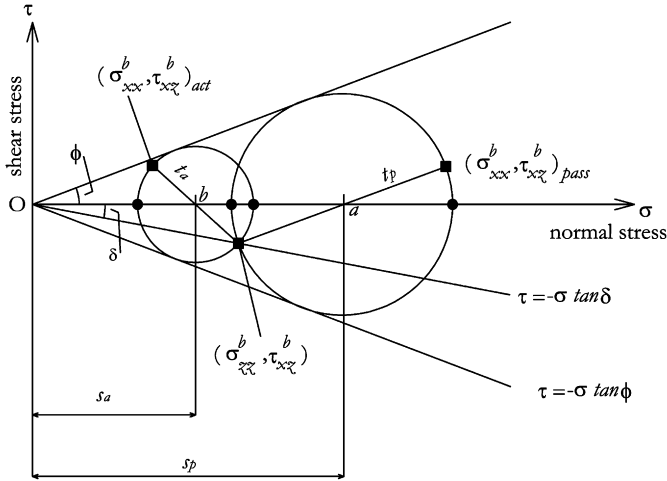


Fig. 8. Mohr-circle-diagram representing the stress state within the avalanche. The yield criterion corresponds to the two straight lines at angles $\pm\phi$ to the horizontal. Similarly, the Coulomb basal dry friction is indicated by the line at an angle $-\delta$ to the horizontal. The passive basal stress state is indicated by the circle of centre a . The circle is both tangent to the yield curves and passes through the point $(\sigma_{zz}, -\sigma_{zz}\tan\delta)$. The circle of centre b represents a second active stress state that also satisfies these conditions. ■ indicate the possible stress states in the xz -plane, ● show possible stress states for σ_{yy} (from Savage and Hutter, 1989).

for the principal stresses, σ_2^b and σ_3^b , there are four values for the basal cross-slope stress σ_{yy}^b .

The earth pressure coefficients K_x^b and K_y^b are defined as follows

$$K_x^b = \frac{\sigma_{xx}^b}{\sigma_{zz}^b}, \quad K_y^b = \frac{\sigma_{yy}^b}{\sigma_{zz}^b} \quad (21)$$

Savage and Hutter (1989) used elementary geometrical arguments to determine the value of K_x^b and Hutter et al. (1993) used the Mohr-circle representation (see Appendix) to define K_y^b as a function of the internal (ϕ) and basal angle (δ) of friction, to derive

$$K_{x_{act/pas}} = 2 \sec^2\phi \left(1 \mp \sqrt{1 - \cos^2\phi \sec^2\delta} \right) - 1 \quad (22)$$

$$K_{y_{act/pas}}^x = \frac{1}{2} \left(K_x + 1 \mp \sqrt{(K_x - 1)^2 + 4 \tan^2\delta} \right) \quad (23)$$

which are real for $\delta \leq \phi$.

To uniquely determine the value of the earth pressure coefficient associated with a particular deformation the earth pressure coefficient K_x is defined to be active or passive according to whether the downslope motion is dilatational or compressional as given by the following equation (Savage and Hutter, 1989)

$$K_x^b = \begin{cases} K_{x_{act}}, & \partial u/\partial x \geq 0 \\ K_{x_{pas}}, & \partial u/\partial x < 0 \end{cases} \quad (24)$$

Analogously, the earth pressure coefficients in the lateral direction are computed by considering whether the downslope and cross-slope deformation are dilatational or compressional

$$K_y^b = \begin{cases} K_{y_{act}}^b, & \partial u/\partial x \geq 0, \partial v/\partial y \geq 0 \\ K_{y_{act}}^b, & \partial u/\partial x \geq 0, \partial v/\partial y < 0 \\ K_{y_{pas}}^b, & \partial u/\partial x < 0, \partial v/\partial y \geq 0 \\ K_{y_{pas}}^b, & \partial u/\partial x < 0, \partial v/\partial y < 0 \end{cases} \quad (25)$$

At the traction free surface of the avalanche the downslope and cross-slope normal surface stresses are

$$\sigma_{xx}^s = 0, \quad \sigma_{yy}^s = 0 \quad (26)$$

Given the values of σ_{xx} and σ_{zz} at the base and the free surface, intermediate values can be now interpolated accordingly. The Savage and Hutter theory assumes that the downslope and cross-slope stresses vary linearly with normal stress through the avalanche depth. This is achieved by the following expression

$$\sigma_{xx} = K_x^b \sigma_{zz}, \quad \sigma_{yy} = K_y^b \sigma_{zz} \quad (27)$$

Substituting the normal stress σ_{zz} with its equation and integrating through the avalanche depth the depth-integrated stresses in the downslope and cross-slope direction are, respectively, given by

$$\bar{\sigma}_{xx} = \rho g K_x^b \gamma_z h/2, \quad \bar{\sigma}_{yy} = \rho g K_y^b \gamma_z h/2 \quad (28)$$

in which, in comparison with terms written in Eq. (6) the K coefficient is included.

According to Hutter et al. (1993), these relations are valid only when the motion is chiefly downhill and the shearing in the (x,y) plane is small in comparison with the shearing in the (x,z) and (y,z) planes. When the sidewise motion is large or when there is strong lateral confinement between rough walls these assumptions break down.

4.2. Original versus modified version of the code

Unlike Hutter et al. (1993), where earth pressure coefficients are defined as the ratio of the longitudinal stresses to the normal stress (see Eq. (21)), the SHWCIN code assumed isotropy of normal stresses, i.e. $\sigma_{xx} = \sigma_{yy} = \sigma_{zz}$.

To relate the depth averaged longitudinal stresses to the depth averaged z direction normal stress a lateral stress coefficient $K_{act/pass}$ has to be used.

As in Iverson and Denlinger (2001), in RASH^{3D} a K coefficient is implemented which applies in the x and y direction simultaneously. Use of a scalar coefficient ensures frame invariance in the x – y plane and preserves the stress symmetry.

The earth pressure coefficient K is considered in the active or passive state, depending on whether the downslope and cross-slope flows are expanding or contracting. The possibility of simultaneous longitudinal contraction and lateral elongation is neglected.

The K coefficient values are given by

$$K_{act/pass} = 2 \frac{1 \mp \sqrt{1 - \cos^2\phi [1 + \tan^2\delta]}}{\cos^2\phi} - 1 \quad (29)$$

where the + (passive state) applies when flow is converging, that is if $\partial_x u + \partial_y v < 0$, and the - (active state) applies when the flow is diverging, that is if $\partial_x u + \partial_y v > 0$.

Earth pressure coefficients, as here defined, modify Eqs. (4) and (5) as follows

$$\frac{\partial}{\partial r}(hu) + \frac{\partial}{\partial x}(hu^2) + \frac{\partial}{\partial y}(huv) = -\gamma_x gh - \frac{\partial}{\partial x}\left(Kg\gamma_z \frac{h^2}{2}\right) - \mu g \gamma_z h \frac{u_x}{\|\mathbf{u}\|} \quad (30)$$

$$\frac{\partial}{\partial r}(hv) + \frac{\partial}{\partial x}(huv) + \frac{\partial}{\partial y}(hv^2) = -\gamma_y gh - \frac{\partial}{\partial y}\left(Kg\gamma_z \frac{h^2}{2}\right) - \mu g \gamma_z h \frac{u_y}{\|\mathbf{u}\|} \quad (31)$$

By using Eq. (29), the K active and passive values are obtained as a function of the value assigned to the basal (δ) and internal (ϕ) friction angles.

The value of K (K_{act} , K_{pass}) to be applied at each point of the mesh is defined as a function of the divergence of the velocity as weighed average by the area of the triangles.

The method can be illustrated on the mesh presented in Fig. 4. For example, through the edge cutting $P_i P_j$ the K value is defined as follows

$$K = \begin{cases} K_{\text{act}}, & \text{div}_{P_i}(\mathbf{u}) > 0, \text{div}_{P_j}(\mathbf{u}) > 0 \\ K_{\text{pass}}, & \text{div}_{P_i}(\mathbf{u}) < 0, \text{div}_{P_j}(\mathbf{u}) < 0 \\ 1, & \text{div}_{P_i}(\mathbf{u}) \cdot \text{div}_{P_j}(\mathbf{u}) \leq 0 \end{cases} \quad (32)$$

5. Validation and observations

5.1. Laboratory test

5.1.1. General description

A laboratory experiment on a chute with a complex basal topography performed by Gray et al. (1999) has been used to test the effect of the earth pressure coefficients.

In the experiment a simple reference surface is defined, which consists of an inclined plane ($\psi = 40^\circ$) that is connected to a horizontal runout zone ($\psi = 0^\circ$) by a cylindrical zone. Superposed on the inclined section of the chute is a shallow parabolic cross-slope topography, $y^2/2R$ with $R = 110$ cm, which forms a channel that partly confines the avalanche motion (Fig. 9).

The inclined parabolic chute lies in $x < 215$ cm, the plane run out zone lies in the range $x > 255$ cm and a transition zone smoothly joins the two regions.

The experiment is performed with quartz chips of mean diameter 2–4 mm, internal angle of friction $\phi = 40^\circ$ and basal angle of friction $\delta = 30^\circ$.

The granular material is released from rest on the parabolic inclined section of the chute by means of a perspex cap that opens rapidly at $t = 0$ s. The cap has a spherical free surface, which is fitted to the basal chute topography. The projection of this line of intersection onto the reference surface is

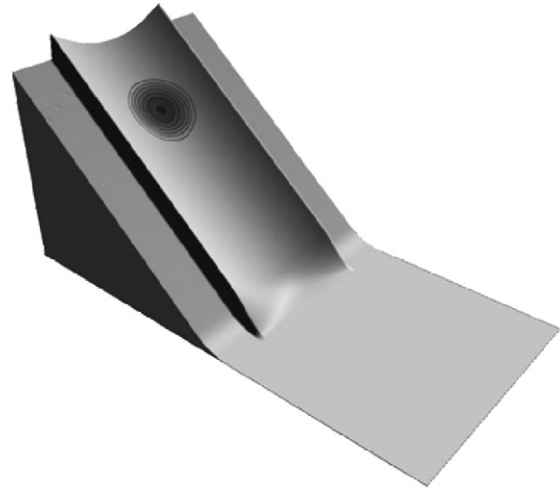


Fig. 9. Experimental apparatus made of a weakly parabolic channel (Image courtesy of S. McDougall, University of British Columbia, Canada).

approximately elliptical in shape. The major axis of the ellipse is of length 32 cm and the maximum height of the cap above the reference surface is 22 cm.

5.1.2. Numerical results

Numerical results obtained by Gray et al. (1999) with a constant bed-friction angle gave results showing that the avalanche tail moved only a few centimetres from its initial position and therefore the shape assumed by the material was more elongated than in the experiments. Results presented in Figs. 10 and 11 show a sequence of pictures at approximately 0.25 s intervals obtained by Gray et al. (1999) using a variable bed-friction angle: in the front quarter of the avalanche the bed-friction angle is assumed constant but reduces linearly in the rear three-quarters.

The vertical lines at $x = 215$ cm and $x = 255$ cm indicate the beginning and the end of the transition zone, respectively. The inclined plane is on the left of each panel and the horizontal run out zone is on the right. The top panel shows the initial configuration of the avalanche and in the subsequent panels an additional thick solid line indicates the position of the experimental avalanche boundary, which provides a direct comparison with the computed boundary of the edge of the shaded domains.

All the analyses carried out with RASH^{3D} assume a constant bed-friction angle. It is preferred to obtain a more detailed correspondence between numerical and experimental results by increasing or decreasing the constant value assigned to the bed-friction angle for each analysis instead of introducing an ad hoc variation of the bed-friction angle.

RASH^{3D} numerical analyses were initially carried out assuming isotropy of normal stresses with a constant basal friction angle $\delta = 30^\circ$ (Fig. 12).

At $t = 0.51$ s the numerical and the experimental results are acceptable even though a difference exists between the real and evaluated position of the front of the mass. The simulated avalanche behaviour is satisfactory along the confined inclined

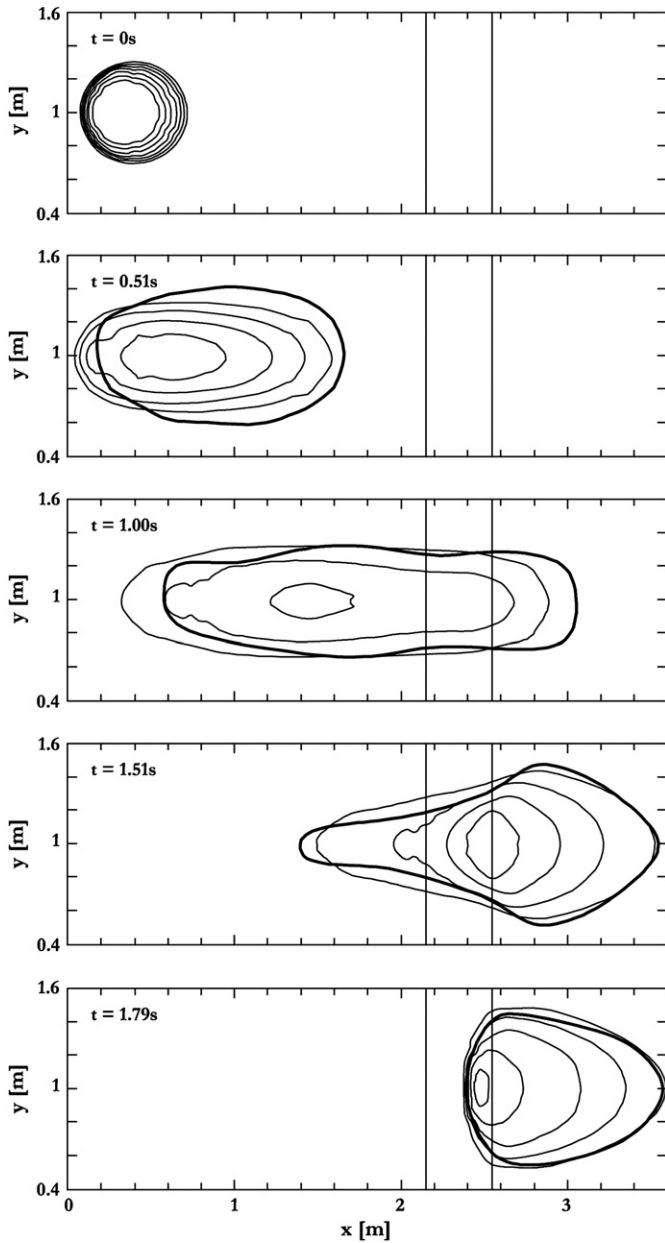


Fig. 10. The computed avalanche thickness is illustrated at five time intervals. The thick solid line indicates the position of the avalanche edge in the laboratory experiment assuming anisotropy of normal stresses (modified from Gray et al., 1999).

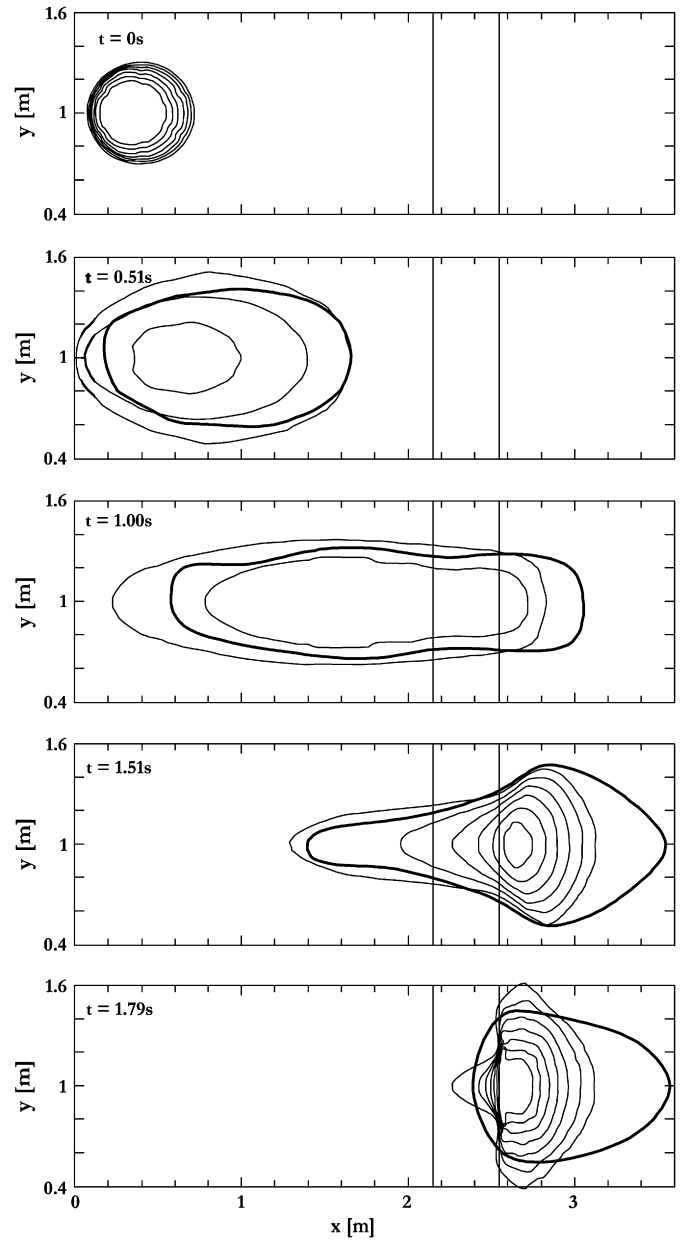


Fig. 11. The computed avalanche thickness is illustrated at five time intervals. The thick solid line indicates the position of the avalanche edge in the laboratory experiment assuming isotropy of normal stresses (modified from Gray et al., 1999).

channel but when the horizontal plane is reached some problems are pointed out. In fact, at $t = 1.00$ s the maximum run out distance is underpredicted and at $t = 1.51$ s results become unacceptable, the deposit becoming too compact (Fig. 12).

A set of analyses assuming $\delta = 27^\circ$ are also run. The obtained results are encouraging up to $t = 1.00$ s, but at $t = 1.51$ s the problem of a too compact deposit is again pointed out (Fig. 12).

If these results are compared to those obtained by Gray et al. (1999) an interesting agreement emerges. In fact, when the avalanche is in divergence the model gives the same behaviour as in the experiment. While, as soon as the avalanche

begins to converge in the run out zone a much more compact deposit is obtained, and the maximum run out distance is underpredicted.

In this frame the analysis of earth pressure coefficients becomes fundamental.

In Table 1 are summarized the K values as a function of the model hypotheses considering an internal friction angle $\phi = 40^\circ$ and a basal friction angle $\delta = 27^\circ$ and $\delta = 30^\circ$, respectively.

As previously mentioned, the Iverson and Denlinger (2001) approach is followed in RASH^{3D}. Two values for K are defined to introduce the anisotropy hypothesis (Table 1 hypothesis 2a).

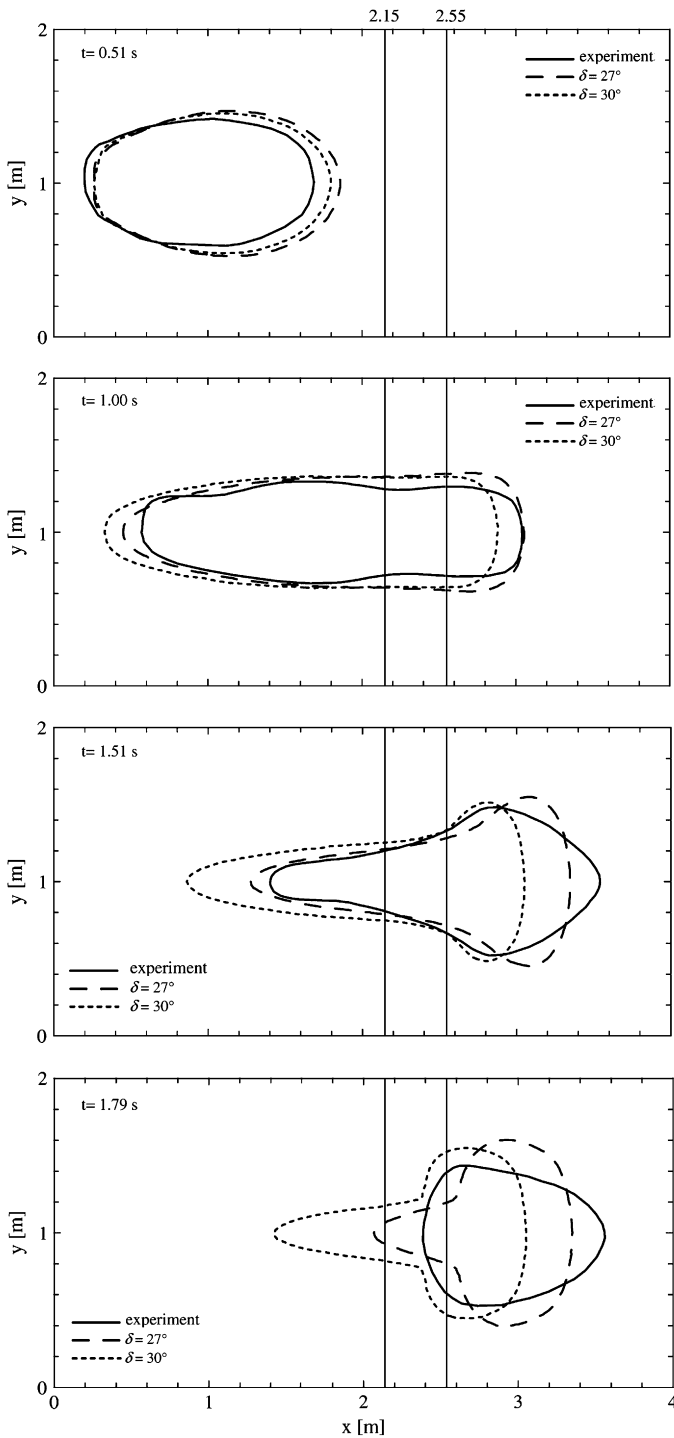


Fig. 12. Analyses carried out with RASH^{3D} assuming isotropy of normal stresses.

In this hypothesis, some interesting aspects emerge comparing results obtained in isotropy ($\delta = 30^\circ$) and anisotropy ($\delta = 30^\circ - \phi = 40^\circ$) conditions (Fig. 13).

At $t = 0.51$ s and $t = 1.00$ s the results underline that the general behaviour of the mass remains approximately the same independently from the assumed hypothesis of isotropy or anisotropy, the front position is overpredicted along the chute and underpredicted when the horizontal plane is gained.

Table 1
Earth pressure coefficients

$\delta = 27^\circ - \phi = 40^\circ$ Earth pressure coefficients			
1. Isotropy $K = 1$			
2. Anisotropy			
a.	$K_{act} = 0.67$	$K_{pass} = 4.15$	
b.	$K_{x,act} = 0.67$	$K_{y,act} = 0.30$	$K_{y,pass} = 1.37$
	$K_{x,pass} = 4.15$	$K_{y,act} = 0.92$	$K_{y,pass} = 4.23$
$\delta = 30^\circ - \phi = 40^\circ$ Earth pressure coefficients			
1. Isotropy $K = 1$			
2. Anisotropy			
a.	$K_{act} = 0.82$	$K_{pass} = 4.00$	
b.	$K_{x,act} = 0.82$	$K_{y,act} = 0.32$	$K_{y,pass} = 1.49$
	$K_{x,pass} = 4.00$	$K_{y,act} = 0.89$	$K_{y,pass} = 4.10$

Values of K defined as a function of the model hypotheses: (1) Isotropy of normal stresses; (2) anisotropy of normal stresses, (a) see Eq. (27) – (b) see Eqs. (20)–(21).

However, it is important to underline that a different trend of the mass behaviour can be pointed out. Along the chute the overprediction is higher when assuming $K = 1$ instead of $K \neq 1$ and on the horizontal plane the underprediction is higher assuming $K = 1$ instead of $K \neq 1$.

From results obtained at $t = 1.51$ s and $t = 1.79$ s it emerges that the difference in the front positions on the horizontal plane becomes large. Assuming $K \neq 1$ the longitudinal position of the distal point approximates in a better way the experimental results but some problems emerge on the deposit width.

A good approximation of the propagation phase was numerically obtained by McDougall and Hungr (2004) using a rheology with $\delta = 27^\circ$ and $\phi = 40^\circ$ and 4 values of K parameter (Table 1 hypothesis 2.b). The predicted distribution of the final deposit is reasonably accurate, with slightly more radial spreading (Fig. 14).

In order to compare the results obtainable with RASH^{3D} to those obtained by McDougall and Hungr (2004), analyses have been also carried out assuming the isotropy condition with $\delta = 27^\circ$ and the anisotropy condition with $\delta = 27^\circ$ and $\phi = 40^\circ$ (Fig. 15).

It emerges that at $t = 0.51$ s a large difference exists in the position reached by the front of the mass in the two hypotheses, even though an overprediction still exists it is higher in case of $K = 1$. At $t = 1.00$ s it seems that in both cases the mass assumes the same behaviour but an important difference is underlined at $t = 1.51$ where by assuming $K \neq 1$ a satisfactory approximation of the longitudinal position assumed by the mass during the experiment is numerically reached. The same is if $t = 1.79$ s is considered.

5.1.3. Observations

In order to try to explain these results, the spatial variation of the earth pressure coefficient K during the propagation phase was obtained by Gray et al. (1999) is quoted in Figs. 16 and 17. The state of stress in down and cross-slope

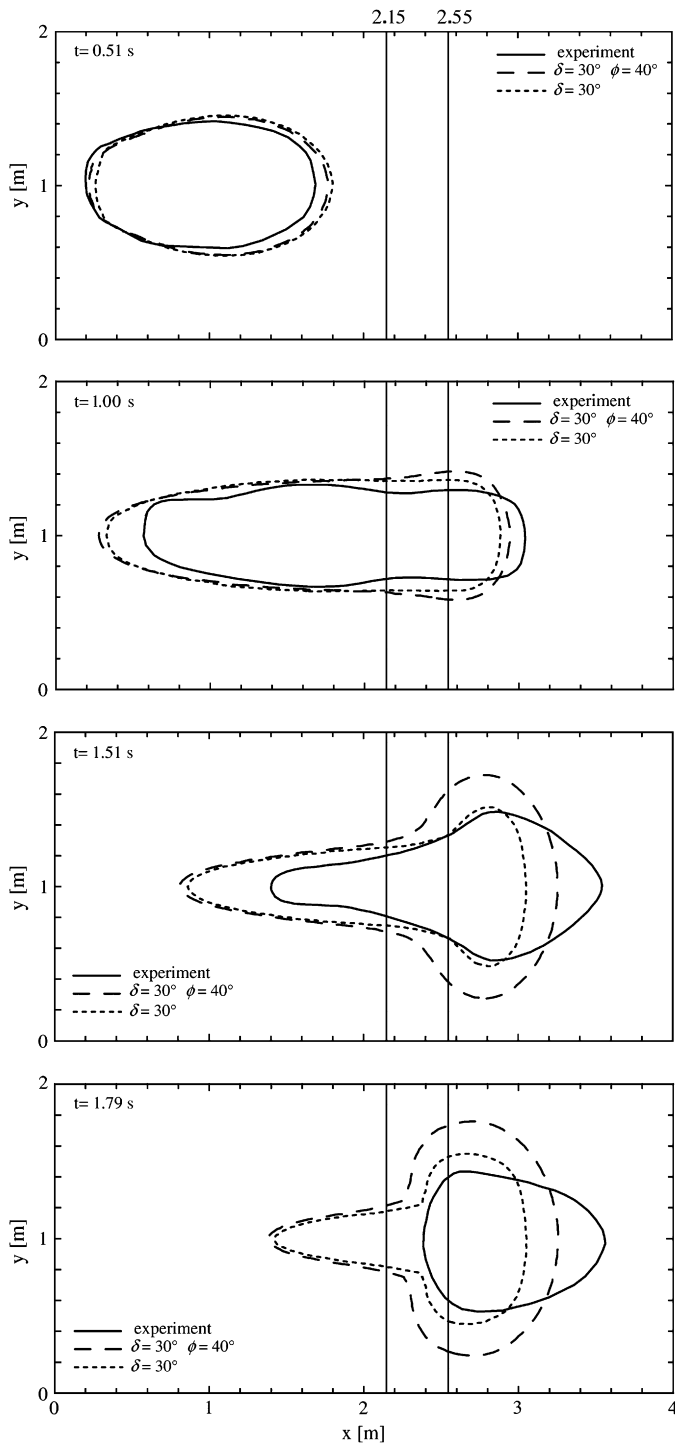


Fig. 13. Comparison between analyses carried out with RASH^{3D} assuming isotropy and anisotropy of normal stresses.

directions is illustrated in the hypothesis of 4 values of the K parameter (as assumed by McDougall and Hungr, 2004). Cells are shaded to show which value of the earth pressure coefficient is activated at any given time.

The highest velocities are attained at the front of the avalanche and this predominantly divergent motion gives rise to active downslope earth pressures at $t = 0.51$ s while in the

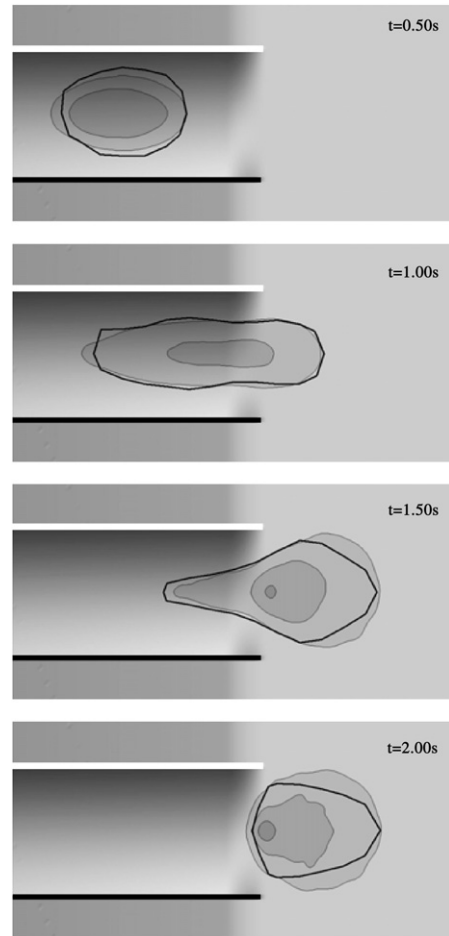


Fig. 14. Analyses of run out experiment carried out by McDougall and Hungr (2004) with anisotropy of normal stresses (Image courtesy of S. McDougall, University of British Columbia, Canada).

cross-slope the transition from expansion to compression originates some active and passive cells.

After 1 s has elapsed the avalanche spans all three sections of the chute and all the earth pressure states in the downslope and cross-slope directions are activated. The front of the avalanche lies on the horizontal plane and diverges in the downslope direction, as does the granular material on the inclined section of the chute. In the run out zone, the lateral confinement ceases, the avalanche is free to expand laterally and the earth pressure coefficients change accordingly.

At 1.51 s the front of the avalanche has virtually come to rest and the whole avalanche is in downslope convergence. In addition, since lateral confinement ceases on the run out plane there is strong cross-slope divergence throughout most of the avalanche, with only the tip of the tail being compressed (Gray et al., 1999).

The model here applied with variation of the earth pressure coefficients considers two values for K . The approach can be considered at least qualitatively correct, limits are probably due to the hypothesis that where $\partial_x u + \partial_y v < 0$ the flow is considered converging and the passive state applies both in x and y directions, if $\partial_x u + \partial_y v > 0$ the active state applies. As

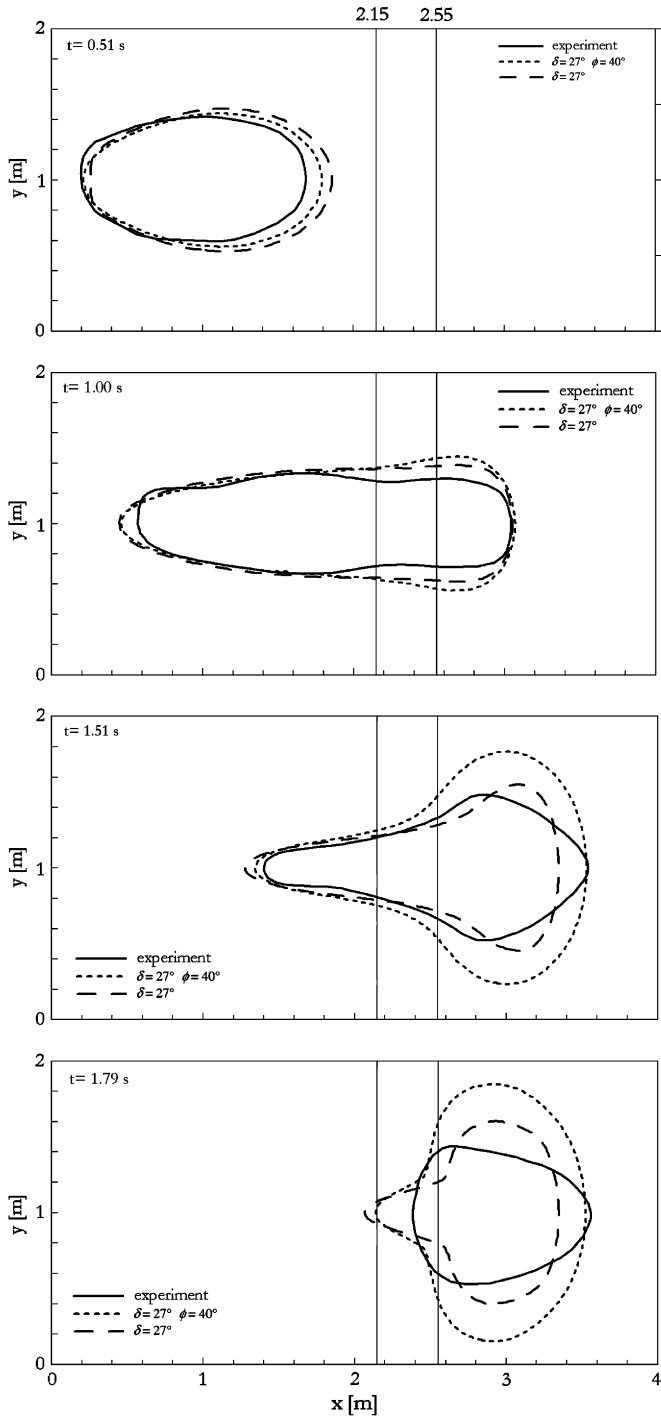


Fig. 15. Comparison between analyses carried out with RASH^{3D} assuming isotropy and anisotropy of normal stresses.

presented in Fig. 18 this approach can originate only two types of mass behaviours: divergence in both directions or convergence in both directions.

At the contrary, if 4 values of K had been considered (see Eqs. (24) and (25)) it would have been possible to have also divergence in a direction and convergence in the other one (Fig. 19).

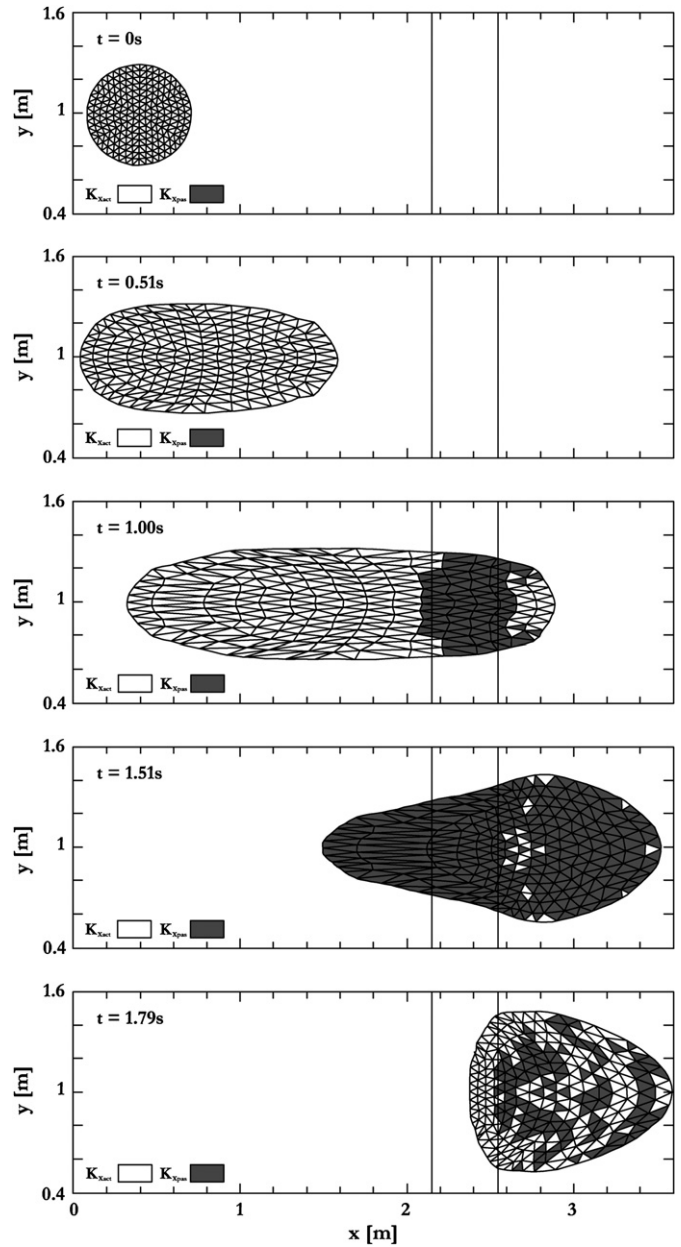


Fig. 16. The value of the downslope earth pressure coefficient (from Gray et al., 1999).

The obtained results are considered encouraging and qualitatively corrects. Differences as to experimental results can be explained, for example in case of $\delta = 30^\circ$ and $\phi = 40^\circ$, as follows.

At $t = 0.51$ s the mass accelerates in downslope direction and the following conditions can be assumed

$$\left| \frac{\partial u}{\partial x} \right| > \left| \frac{\partial v}{\partial y} \right|; \frac{\partial u}{\partial x} > 0 \quad (33)$$

Considering the hypothesis 2a (Table 1, anisotropy with 2 values of K) $\partial_x u + \partial_y v > 0$ is obtained and $K_{act} = 0.82$ is applied in downslope and cross-slope directions. If the

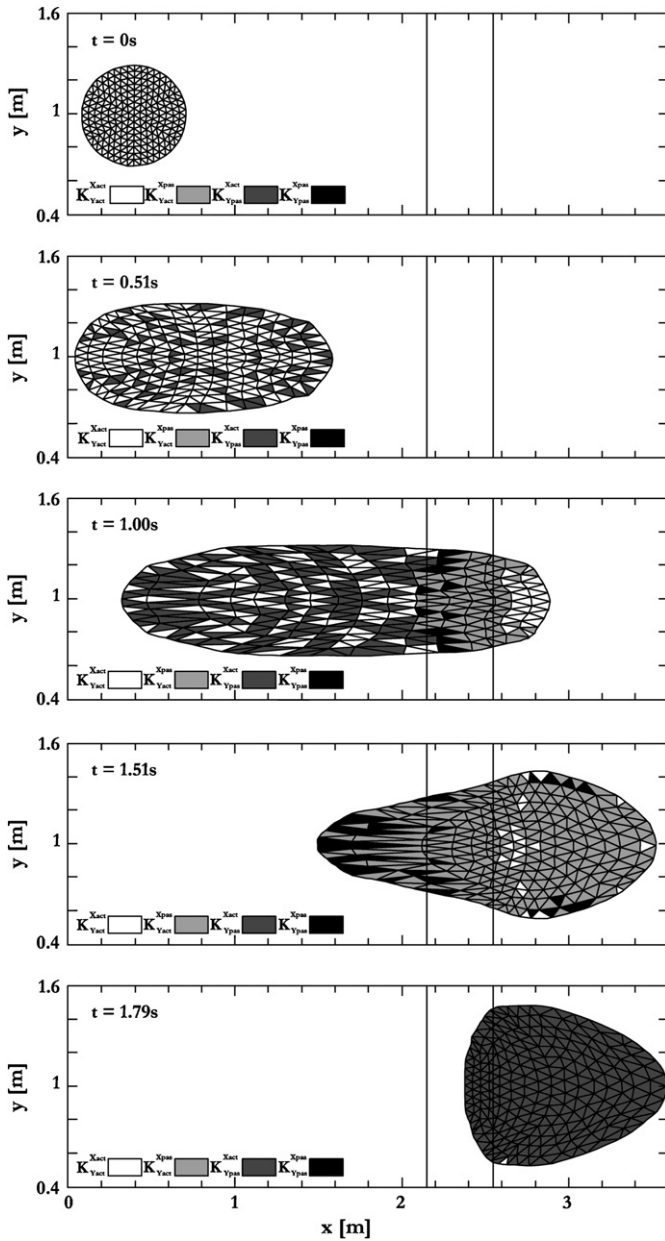


Fig. 17. The value of the cross-slope earth pressure coefficient (from Gray et al., 1999).

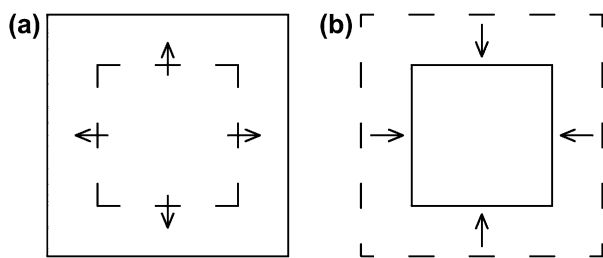


Fig. 18. Simultaneous longitudinal and lateral elongation (a) and longitudinal and lateral contraction (b).

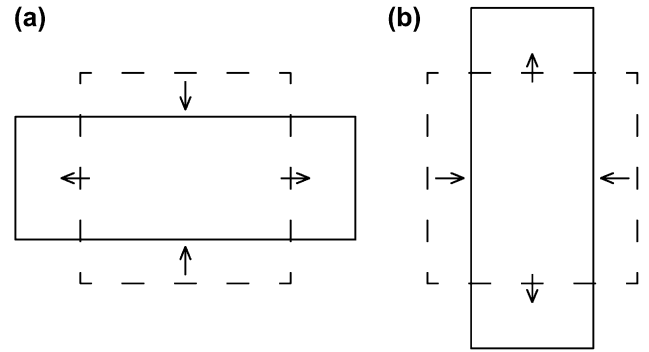


Fig. 19. Simultaneous longitudinal elongation and lateral contraction (a) and longitudinal contraction and lateral elongation (b).

hypothesis 2b (Table 1, anisotropy with 4 values of K) is considered, the K value in downslope direction is the same than in case 2a, and approximately the same used in case of isotropy, but in cross-slope direction it is possible to have $K = K_{act} = 0.32$ or $K = K_{pass} = 1.49$. This can modify the width of the mass along the chute.

At $t = 1.00$ s three phases can be considered

$$\text{Chute } \left| \frac{\partial u}{\partial x} \right| > \left| \frac{\partial v}{\partial y} \right|; \frac{\partial u}{\partial x} > 0 \frac{\partial v}{\partial y} < 0; \partial_x u + \partial_y v > 0 \quad (34)$$

$$\text{Transition zone } \left| \frac{\partial u}{\partial x} \right| > \left| \frac{\partial v}{\partial y} \right|; \frac{\partial u}{\partial x} < 0 \frac{\partial v}{\partial y} > 0; \partial_x u + \partial_y v < 0 \quad (35)$$

$$\text{Horizontal plane } \frac{\partial u}{\partial x} > 0 \frac{\partial v}{\partial y} > 0; \partial_x u + \partial_y v > 0 \quad (36)$$

Along the chute, as in case of $t = 0.51$ s, in cross-slope direction there are both active and passive cells but elements passive in y and active in x are in prevalence. To consider in



Fig. 20. Frank slide.

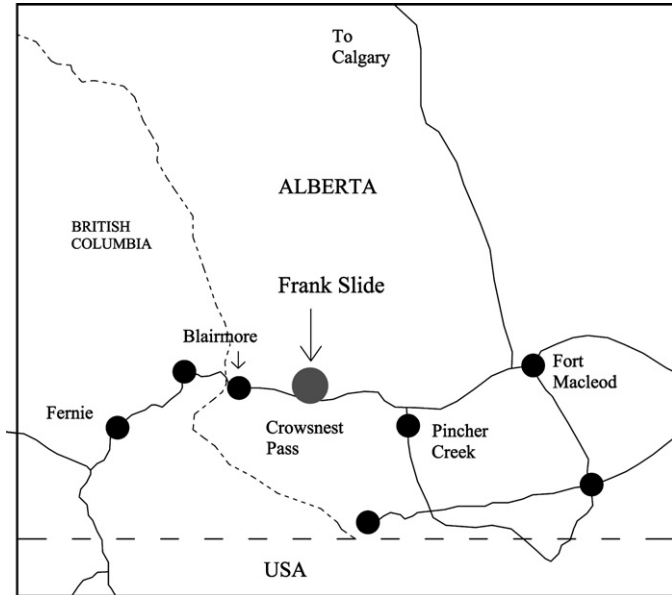


Fig. 21. Location of the Frank slide area.

the propagation only in the downslope direction while in the cross-slope $K = 0.32$ is assumed and, in fact, the width is correctly reduced.

At $t = 1.51$ s the mass decelerates in downslope direction and the following conditions can be assumed

$$\left| \frac{\partial u}{\partial x} \right| > \left| \frac{\partial v}{\partial y} \right|; \frac{\partial u}{\partial x} < 0 \quad (37)$$

Considering the hypothesis 2a $\partial_x u + \partial_y v < 0$ is obtained and $K_{\text{pass}} = 4.00$ is applied in downslope and cross-slope directions. If the hypothesis 2b is considered the K value in downslope direction is the same than in case 2a but in cross-slope direction it is $K = K_{\text{act}} = 0.79$ and the width becomes correctly reduced.

The condition $t = 1.79$ s is complex, there are active and passive cells but the general behaviour determine a prevalence of active values in cross-slope direction that reduces spreading of the mass.

The graphic comparison between isotropy and anisotropy results helps to underline that it is useful to split the K value in x and y directions. In fact, values as $K \cong 4$ allow reproducing the position of the front but in the cross-slope direction becomes fundamental to use $K \leq 1$.

the transition zone only one K value in both x and y directions does not allow to underline distinction between convergence and divergence. On the horizontal plane the hypothesis 2a gives a $K = 0.82$ while in the hypothesis 2b $K = 0.82$ defines

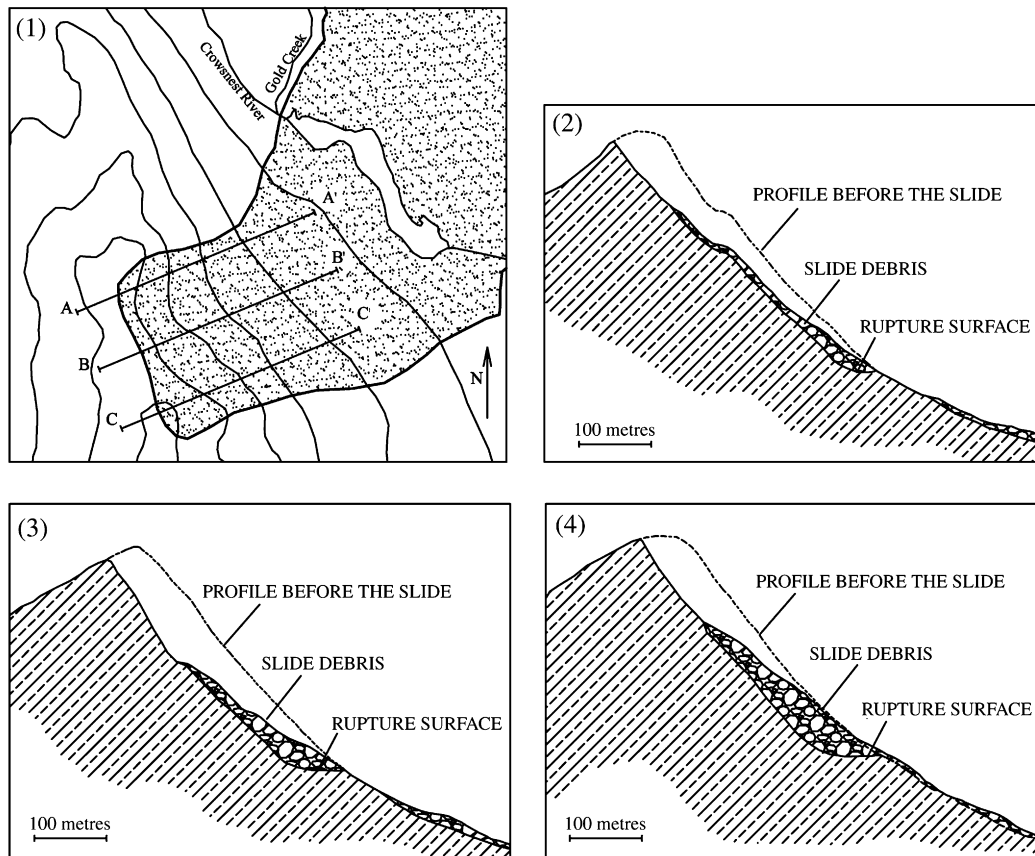


Fig. 22. Frank slide. (1) Map of the Turtle Mountain area. (2) Cross-section through Turtle Mountain along line A–A'. (3) Cross-section through Turtle Mountain along line B–B'. (4) Cross-section along Turtle Mountain along line C–C' (modified from Cruden and Krahn, 1978).

5.2. Frank slide (1903, Canada)

5.2.1. General description

A detailed description of the Frank slide is reported in Cruden and Krahn, 1978, while the short information given in the present paper is set out only to define the general characteristics and the dynamic of the considered avalanche in order to better understand choices made when back analyses are carried out.

The Frank slide occurred on the morning April 29, 1903 (Fig. 20). Frank, a coal mining town of south western Alberta (Canada), located 21 km east of the border with British Columbia and 56 km north of the United States border is today an old townsite (Fig. 21). The new town of Frank is about 2 km north of the old one.

The original rock mass volume is estimated at about $30 \times 10^6 \text{ m}^3$ but the dimensions of the slide are not accurately known because no maps existed of the area before the slide. In Fig. 22 the reconstruction of the failed rock mass along three section lines as made by the experts is given. Reconstruction suggested slab thickness up to 150 m.

The structure of Turtle Mountain was described as a monocline of Paleozoic limestones dipping at about 50° . The slide probably took place on bedding surfaces with orientation of the scarp and lateral margins of the slide controlled by joints sets. A surface of rupture close to the toe of the slide followed a minor thrust above the Turtle Mountain fault.

The slide debris moved down from the east face of Turtle Mountain across the entrance of the Frank mine of the Canadian American Coal Co., the Crowsnest River, the southern end of the town of Frank, the main road from the east, and the Canadian Pacific mainline through the Crowsnest Pass (Fig. 23).

The separated rock mass seems to have been shattered by impacts against the side of the mountain during its descent, and probably long before it reached the bottom, into myriads of fragments, some of which were flung far out into the valley.

The slide rock consists mostly of angular fragments of limestone, ranging in size from grains up to great blocks 12 m in length. Large rocks are common everywhere, especially along the central portion of the slide.

In portions of the slide the space between the rocks are filled with material resembling boulder clay and a number of small mud flats are also present.

In confirmation of this, the reconstruction of the Canadian Pacific Railway line created a cut up to 16 m high across the deposit, giving a unique cross-section nearly the depth of the debris. The debris shows vertical sorting. The base material is crushed limestone, mainly of sand and gravel size, and contains rounded pebbles from till or alluvial deposits on the surface of separation. The upper surface of the debris is an accumulation of large, predominantly angular boulders. Grain-size analyses demonstrate a gradual increase in grain size with height above the base of the cut. Such inverse grading with fines concentrated at the base of the debris indicates that the landslide was not fluidized by gas pore pressure (Cruden and Hungr, 1986).

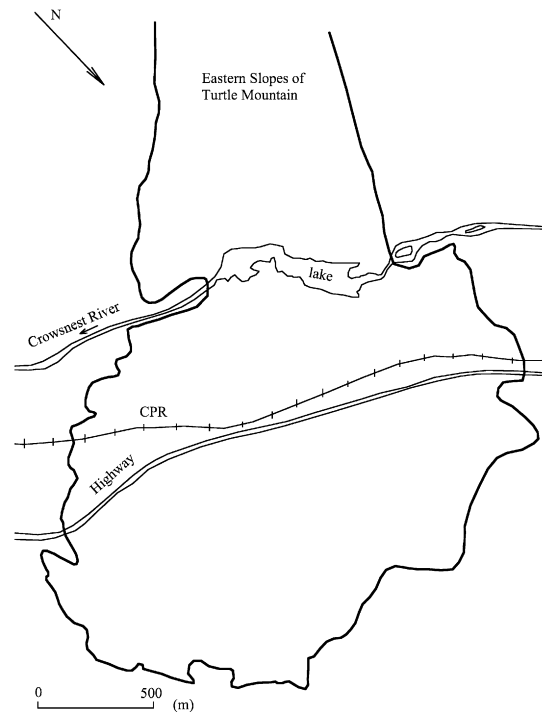


Fig. 23. Plan of the Frank slide debris deposit from an overlay on the National Air Photo Library's vertical air photo A 13077-102 (from Cruden and Hungr, 1986).

In general, the great mass ploughed through the bed of the river and carrying both water and underlying sediments along with it, crossed the valley, climbed 145 m up the opposite side of the valley and finally came to rest 120 m above the valley floor with an average thickness of the debris at 13.7 m over an area of about 3 km^2 .

It is difficult to reach any definite conclusion in regard to the time occupied by the slide, as the estimates of eye witnesses range all the way from 20 s to 2 min.

No estimate of the rate at which the material travelled after it broke away can be given, but as those awakened by the roar had scarcely time to do more than to rise from their beds before all was over, it must have been extremely rapid (McConnell and Brock, 1904).

The number of people killed by the slide is not known exactly, but it is given at about 70. Three-quarters of the homes in Frank were crushed like balsa wood; the people occupying the houses in the track of the slide were all swept away with it and destroyed. The track of the Canadian Pacific Railway was hopelessly buried for a distance of nearly 2000 m. and the river became a lake. The entrance and buildings of the coal mining at the base of Turtle Mountain were buried. Seventeen miners trapped inside performed an astonishing self-rescue. They tunnelled upwards and broke through the surface on the face of the mountain.

For many years, Frank was the only well-described, historic example of what Varnes (1978) called a rockslide-avalanche.

Immediately after the slide an inspection was made by the Geological Survey of Canada. Their report gave a general

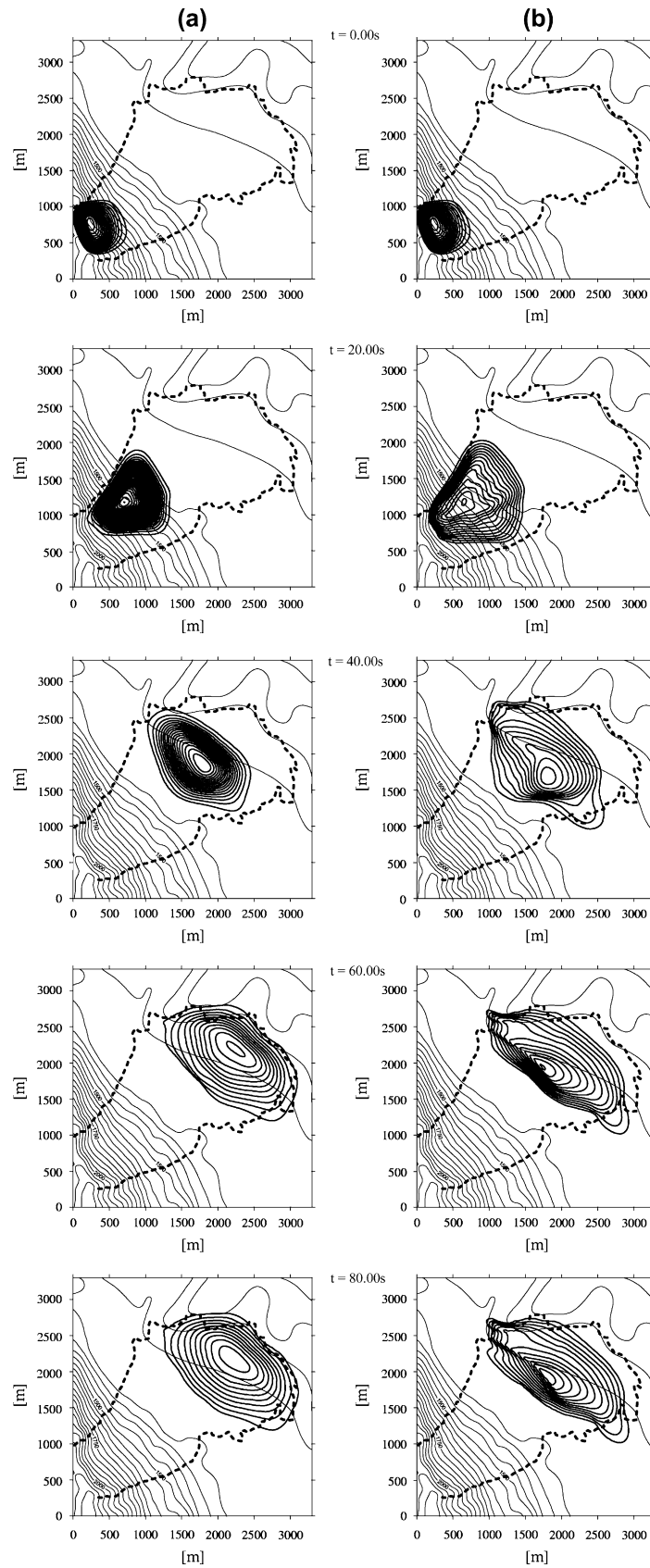


Fig. 24. Analysis of the Frank slide with RASH^{3D}. Plan of the simulated flow position at 20 s intervals (0 s–20 s–40 s–60 s–80 s) in condition of (a) anisotropy and (b) isotropy of normal stresses. The flow depth contours are at 3 m intervals. The sliding surface contours are at 50 m intervals. The dashed line indicated the extent of the real event.

survey of the geology of the mountain. They concluded that the slide occurred across rather than along bedding planes and believed that the primary cause for the slide was to be found in the structure of the mountain. In their opinion any further danger of slides came from the north peak (Cruden and Krahn, 1978) since its structure is similar to the portion which fell away.

On the other hand, people pointed to the role of the mine as one of the causes of the catastrophe. Water action in summit cracks and severe weather conditions may have also contributed to the disaster.

5.2.2. Numerical results

No before-event maps existed of the area affected by the Frank slide but using detailed digital elevation data provided by the Geological Survey of Canada as well as historical photographs and maps, experts had been able to give a reconstruction of the topography and an estimate of volume involved together with boundaries of the triggering area.

A complex rheology should be used given the complexity of the analysed event and the high heterogeneity of the type of material involved. On the other hand it would be impossible to calibrate the high number of parameters that a complex rheology requires (see Pirulli, 2005).

The aim of this work is to have a tool that is applicable to the back analysis of real cases, where a detailed description is usually difficult to be obtained, and the prediction of the evolution of a potential event. For these reasons the motion of the avalanche has been simulated turning to a simple frictional model in which the only rheological parameter to be set is the basal friction angle (δ) and the internal friction angle (ϕ) in case of anisotropy of normal stresses.

RASH^{3D} has been applied using a frictional rheology both in the hypothesis of isotropy and of anisotropy of stresses. Results obtained assuming a basal friction angle $\delta = 14^\circ$ and a $\phi = 40^\circ$ in case of anisotropy have been compared. A so low value of the basal friction angle can be considered index of heterogeneity of the involved material and of influence of water on propagation, which is not known in this case.

In Fig. 24 results are compared superposing the obtained runout of the mass with RASH^{3D}, in the assumed hypotheses of both isotropy and anisotropy, on the boundaries of the area as surveyed on site.

Numerical results clearly underline a difference in the behaviour assumed by the mass during propagation. It is not easy to say which behaviour can be considered as more realistic but from the analysis of the different recorded frames it emerges that in case of anisotropy the material assumes a more compact and regular behaviour (Fig. 24a) than in case of isotropy (Fig. 24b).

6. Conclusions

The SHWCIN code has been extended in this paper to model the flow of granular avalanches over a complex three-dimensional topography. This has been achieved by changing

the type of the adopted mesh, from structured to unstructured, and by implementing the code so that the effect of a real topography on the gravity vector components can be taken into account.

The SHWCIN code has the possibility of analysing the propagation of a fluid with an earth pressure coefficient K always equals 1. As previously explained, if the bulk of the flowing mass is a dry granular material with friction, the coefficient K may range between the active and passive coefficient K_{act} and K_{pass} and this can widely modify the avalanche shapes; as it controls how much spreading and contraction occur.

The SHWCIN code has been upgraded. The obtained new code (RASH^{3D}) gives the possibility of using, as in Iverson and Denlinger (2001), a K coefficient which applies in the x and y direction simultaneously. Use of a scalar coefficient ensures frame invariance in the x – y plane and preserves the stress symmetry.

To compare the difference among results obtainable in condition of both isotropy and anisotropy, the RASH^{3D} code has been applied in case of a laboratory experiment and a back analysis of the case history of Frank slide.

In both cases, differences due to the K coefficient mainly emerge when the topography does not constrain the mass to follow a given path. That is, when the mass abandons the inclined parabolic chute and gains the horizontal plane in case of the laboratory apparatus and when the mass abandons the slope and reaches the flat bottom of the valley in case of the real slide.

It is underlined that to determine a general converging or diverging condition of the whole mass is not enough. To guarantee best results it would be important to apply a different K value, at the same time, along directions of convergence and directions of divergence.

Further developments of the research work undertaken are needed. These have to be done by keeping in mind the final objective, which is to provide a tool whose application could give useful information for investigating, within realistic geological contexts, the dynamics of real flows and of their arrest phase.

Acknowledgements

The authors wish to acknowledge Dr. Scott McDougall and Professor Oldrich Hungr for having provided us data concerning the Frank slide and for the fruitful discussions.

Appendix

Stress tensor is defined in the reference frame (x, y, z) introduced in Fig. 3. It is assumed that the Mohr circle tangential to the failure envelope is that describing the stress state in the xz -plane and that $\tau_{xz} = -\sigma_{xx} \tan \delta$, with δ the basal friction angle. In Mohr plane, the failure envelope, assuming a Coulomb-type behaviour with cohesion equal to zero and internal friction angle ϕ , is a line passing through the origin O and having dip equal to ϕ .

Two circles pass through the point $(\sigma_{zz}, \sigma_{zz} \tan \delta)$ and are tangent to the failure envelope, as it is underlined in Fig. 8.

Assuming s and t as the coordinate of the centre of the circle along the σ -axis and the radius of the circle, respectively, conditions of tangency and of passage through $(\sigma_{zz}, \sigma_{zz} \tan \delta)$ can be written as follows

$$t = s \sin \phi \quad (38)$$

$$\sigma_{zz}^2 + (\sigma_{zz} \tan \delta)^2 = t^2 \quad (39)$$

Solving the system of Eqs. (38) and (39), two solutions are obtained

$$s = \frac{1}{\cos^2 \phi} \left(1 \pm \sqrt{1 - \frac{\cos^2 \phi}{\cos^2 \delta}} \right) \sigma_{zz} \quad (40)$$

$$t = \frac{\sin \phi}{\cos^2 \phi} \left(1 \pm \sqrt{1 - \frac{\cos^2 \phi}{\cos^2 \delta}} \right) \sigma_{zz} \quad (41)$$

where $+$ corresponds to the passive state and $-$ to the active state.

Earth pressure coefficients in the direction of steepest descent can then be obtained as follows

$$K_{x,act/pass} = \frac{\sigma_{xx}}{\sigma_{zz}} = \frac{2s - \sigma_{zz}}{\sigma_{zz}} = \frac{2}{\cos^2 \phi} \left(1 \mp \sqrt{1 - \frac{\cos^2 \phi}{\cos^2 \delta}} \right) - 1 \quad (42)$$

Due to the hypotheses of a cross-slope stress that is principal ($\sigma_{yy} = \sigma_1$) and that is equal to one of the other principal stresses acting in the (x,z) -surface ($\sigma_1 = \sigma_2$) it is possible to obtain K_y as follows

$$K_y = \frac{\sigma_{yy}}{\sigma_{zz}} = \frac{\sigma_1}{\sigma_{zz}} = \frac{\sigma_2}{\sigma_{zz}} \quad (43)$$

Since σ_2 is defined as quoted in Eq. (20), K_y becomes

$$K_{y,act/pass}^x = \frac{1}{2} \left(K_x + 1 \mp \sqrt{(K_x - 1)^2 + 4 \tan^2 \delta} \right) \quad (44)$$

References

- Audusse, E., Bristeau, M.O., Perthame, B., 2000. Kinetic Schemes for Saint-Venant Equations with Source Terms on Unstructured Grids. INRIA Rep. 3989. National Institute for Research in Computer Science and Control, Le Chesnay, France.
- Audusse, E., Bristeau, M.O., 2005. A well-balanced positivity preserving "second-order" scheme for shallow water flows on unstructured meshes. *Journal of Computational Physics* 206, 311–333.
- Bristeau, M.O., Coussin, B., Perthame, B., 2001. Boundary Conditions for the Shallow Water Equations Solved by Kinetic Schemes. INRIA Rep. 4282. National Institute for Research in Computer Science and Control, Le Chesnay, France.
- Chen, H., Lee, C.F., 2000. Numerical simulation of debris flows. *Canadian Geotechnical Journal* 37, 146–160.
- Cruden, D.M., Krahn, J., 1978. Frank rockslide, Alberta, Canada. In: Barry, V. (Ed.), *Rockslides and Avalanches. Natural Phenomena. Chapter 2, vol. 1.* Elsevier Scientific Publishing Company, Amsterdam, pp. 97–112.
- Cruden, D.M., Hungr, O., 1986. The debris of the Frank Slide and theories of rockslide–avalanche mobility. *Canadian Journal of Earth Sciences* 23, 425–432.
- Cundall, P.A., 1988. Computer simulations of dense sphere assemblies. In: Satake, M., Jenkins, J.T. (Eds.), *Micromechanics of Granular Material.* Elsevier Science Publishers, Amsterdam, pp. 113–123.
- Denlinger, R.P., Iverson, R.M., 2004. Granular avalanches across irregular three-dimensional terrain: 1. Theory and computation. *Journal of Geophysical Research* 109.
- Gray, J.M.N.T., Wieland, M., Hutter, K., 1999. Gravity-driven free surface flow of granular avalanches over complex basal topography. In: *Proceedings of the Royal Society of London, Series A* 455 (1841).
- Hutter, K., Siegel, M., Savage, S.B., Nohguchi, Y., 1993. Two-dimensional spreading of a granular avalanche down a inclined plane. Part I. *Acta Mechanica* 100, 37–68.
- Hungr, O., 1995. A model for the runout analysis of rapid flow slides, debris flows, and avalanches. *Canadian Geotechnical Journal* 32, 610–623.
- Iverson, R.M., Denlinger, R.P., 2001. Flow of variably fluidized granular masses across three-dimensional terrain. A. Coulomb mixture theory. *Journal of Geophysical Research* 106, 537–552.
- Mangeney-Castelnau, A., Vilotte, J.-P., Bristeau, M.O., Perthame, B., Bouchut, F., Simeoni, C., Yernini, S., 2003. Numerical modelling of debris avalanche based on Saint-Venant equations using a kinetic scheme. *Journal of Geophysical Research* 108 (B11), 1–18. EPM 9.
- McConnell, R.G., Brock, R.W., 1904. Report on the Great Landslide at Frank, Alberta. Annual Report 1903, part 7. Department of the Interior (Canada), 17 pp.
- McDougall, S., Hungr, O., 2004. A model for the analysis of rapid landslide runout motion across three-dimensional terrain. *Canadian Geotechnical Journal* 41 (6), 1084–1097(14).
- Pirulli, M., 2005. Numerical modelling of landslide runout, a continuum mechanics approach. Ph.D. thesis in Geotechnical Engineering, Supervisor: Prof. Scavia Claudio, Politecnico di Torino, Italy.
- Savage, S.B., Hutter, K., 1989. The motion of a finite mass of granular material down a rough incline. *Journal of Fluid Mechanics* 199, 177–215.
- Savage, S.B., Hutter, K., 1991. The dynamics of granular materials from initiation to runout. *Acta Mechanica* 86, 201–223.
- Strack, O.D.L., Cundall, P.A., 1984. Fundamental Studies of Fabric in Granular Materials. Interim Report to NSF. CEE-8310729. Department of Civil and Mineral Engineering, University of Minnesota, Minneapolis, Minnesota.
- Varnes, D.J., 1978. Slope movement types and processes. In: Schuster, R.J., Krizek, R.J. (Eds.), *Landslides, Analysis and Control: Transportation Research Board. National Academy of Sciences, Washington DC*, pp. 11–33. Special Report 176.
- Walton, O.R., Braun, R.L., Mallon, R.O., Correlli, D.M., 1988. Particle-dynamics calculations of gravity flows of inelastic, frictional spheres. In: Satake, M., Jenkins, J.T. (Eds.), *Micromechanics of Granular Material.* Elsevier Science Publisher, Amsterdam, pp. 153–161.
- Will, J., Konietzky, H., 1998. Neue Techniken der Numerik zur Berechnung von Felsböschungen. *Felsbau* 16, 155–167.
- Wilkinson, P.L., Anderson, M.G., Lloyd, D.M., Renaud, J.-P., 2002. Landslide hazard and bioengineering: towards providing improved decision support through integrated numerical model development. *Environmental Modelling and Software* 17, 333–344.